Blocking layer of dark current for Si-based short-wave infrared photodetection ⊘

Liang Yu [iD] ; Li Wu [iD] ; Xiyuan Dai; Yanru Yang; Zhongyao Yan [iD] ; Kaixin Liu [iD] ; Fengyang Ma [iD] ;
Ming Lu [✉] [iD] ; Jian Sun [✉] [iD]

Check for updates

View Online   Export Citation

Articles You May Be Interested In

Transferable GeSn ribbon photodetectors for high-speed short-wave infrared photonic applications

J. Vac. Sci. Technol. B (June 2024)

Spectrally selective photodetection in the near-infrared with a gold grating-based hot electron structure

Appl. Phys. Lett. (April 2020)

Temperature-dependent photodetection behavior of AlGaN/GaN-based ultraviolet phototransistors

Appl. Phys. Lett. (February 2022)

Applied Physics Letters
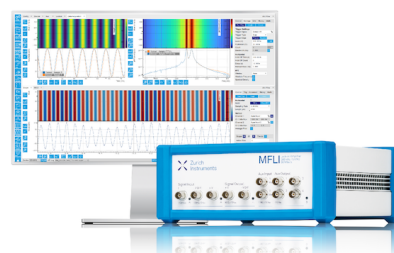
Blocking layer of dark current for Si-based short-wave infrared photodetection

Liang Yu,[1] (iD) Li Wu,[1] (iD) Xiyuan Dai,[1] Yanru Yang,[1] Zhongyao Yan,[1] (iD) Kaixin Liu,[1] (iD) Fengyang Ma,[1] (iD) Ming Lu,[1,2,a]) (iD) and Jian Sun[1,2,a]) (iD)

AFFILIATIONS

[1]Department of Optical Science and Engineering, School of Information Science and Technology, State Key Laboratory of Photovoltaic Science and Technology, and Shanghai Ultra-Precision Optical Manufacturing Engineering Center, Fudan University, Shanghai 200433, China
[2]Yiwu Research Institute of Fudan University, Yiwu, 322000 Zhejiang, China

[a])Authors to whom correspondence should be addressed: minglu55@fudan.edu.cn and jsun@fudan.edu.cn

ABSTRACT

Effective suppression of dark current is essential for improving the performance of bulk defect-mediated absorption (BDA) photodetectors. Blocked impurity band (BIB) infrared detectors have been developed and utilized from mid-infrared to far-infrared wavelength regions for low noise. In this work, a blocking layer of dark current was applied to a BDA short-wave infrared (SWIR) photodetector, emulating the concept of BIB detectors. ZnO was chosen as the blocking layer to impede the transport of electrons from the bulk defect levels due to its wide bandgap and to allow the photocurrent to remain nearly unaffected by proper positioning of the conduction band minimum. After introducing the ZnO blocking layer, the dark current density of the photodetector was reduced by two orders of magnitude, and the specific detectivity was enhanced by one order of magnitude. The effects of TiO_2 and WO_3 as blocking layers were also investigated and compared with ZnO. This work offers an effective method for enhancing detectivity in SWIR BDA photodetection by suppressing the dark current efficiently.

Published under an exclusive license by AIP Publishing. https://doi.org/10.1063/5.0226677

Silicon photonics holds significant research value and application potential in the current semiconductor industry.[1] One crucial component of silicon photonics is the operation of Si-based short-wave infrared (SWIR) photodetectors (PDs),[2] which play important roles in fields such as communications,[3] sensing,[4] biomedical testing,[5] and night vision imaging because of their compatibility with complementary metal–oxide–semiconductor (CMOS) technology.[6,7] Although other novel materials-based SWIR PDs have been developed recently,[8–12] Si-based SWIR PDs remain a highly desired option for its cost-effectiveness and CMOS compatibility.

Due to the 1.12 eV bandgap of Si, it cannot absorb light at SWIR wavelengths larger than 1100 nm.[7,13] Currently, there are several methods to extend its absorption spectrum to the SWIR region,[13,14] including surface-state absorption,[15] internal photoemission effect,[16] two-photon absorption,[17] surface defect-mediated absorption,[18] and bulk defect-mediated absorption (BDA).[19–22] Among these, BDA Si-based PDs usually exhibit high SWIR absorption due to the sub-bandgap absorption mediated by defect levels after doping metallic or nonmetallic ions,[23–27] providing high responsivity for PDs. However, the dark current of the BDA PDs is typically significant, which hinders the improvement of the detectivity of SWIR PDs.[20,28]

After the first demonstration by Petroff and Stapelbroek,[29] blocked impurity band (BIB) infrared BDA PDs have found extensive applications in the field of astronomical detection.[30–32] By introducing a blocking layer to the PD to suppress the transport of electrons from the defect band, the dark current has been effectively reduced. Currently, BIB detectors have been utilized from mid-infrared to far-infrared wavelength region.[33,34]

In this work, in terms of the concept of BIB for mid-infrared and far-infrared detection, a blocking layer was applied for a SWIR BDA silicon-based PD to reduce the dark current. As the primary structure of the PD, Pt was doped into Si to form bulk defects.[35] Furthermore, considering its wide bandgap and its conduction band minimum (CBM) very close to that of Si so that dark current can be effectively suppressed while the photocurrent remains nearly unaffected,[36–38] a ZnO thin film was introduced as a blocking layer of dark current. We compared the inhibitory effect on the dark current of blocking layers with different thicknesses and annealing temperatures of ZnO. Additionally, the impacts of TiO_2 and WO_3 with similar electronic structures and energy level positions to ZnO were also studied as blocking layers and compared to ZnO. This study demonstrates that by applying a blocking layer of dark current to SWIR BDA PD, the

dark current can be reduced significantly, leading to a pronounced enhancement of detectivity.

Double-side polished single crystal Si wafers ($10 \times 10 \times 0.2 \, mm^3$ in size, n-type, $1–5 \, \Omega \, cm$) were chosen as substrates for the PDs. Initially, the Si wafers were ultrasonically cleaned in acetone, ethanol, and de-ionized water sequentially for 15 min to remove surface contamination. Then, the wafers were cleaned by the RCA process. The Si wafers were rinsed into a mixed solution consisting of $(NH_3 \cdot H_2O)/H_2O_2/H_2O$ in a 1:1:5 ratio at 70 °C for 20 min and $HCl/H_2O_2/H_2O$ in a 1:1:6 radio at 70 °C for 10 min in sequence to remove surface impurities.[39,40] Finally, the Si wafers were dipped in 1% HF for 1 min to remove the native surface oxide.

A 10 nm thick Pt film was deposited on the rear side of the Si substrate using magnetron sputtering at a power of 86.4 W in an Ar atmosphere of 0.5 Pa. Then, the Si with the Pt film was annealed at 950 °C for 30 min in nitrogen, facilitating the diffusion of Pt into the Si and the formation of bulk defects. Next, a 40 nm thick ZnO, TiO_2, or WO_3 layer was deposited onto the rear side of Pt-doped Si by atomic layer deposition (ALD) at 200, 200, or 300 °C, respectively. Following this process, the samples were annealed in nitrogen at 600 °C for 30 min. A 150 nm thick ITO film was deposited on the front side of the sample by electron beam evaporation as the front electrode, and a 5 μm thick Al film was deposited on the rear side of the sample using thermal evaporation as the rear electrode. The entire device was finally annealed at 450 °C in nitrogen for 5 min to form ohmic contacts between the electrodes and the sample. Figures 1(a) and 1(b) present a schematic illustration of the PD and its cross-sectional scanning electron microscopy (SEM) image, respectively.

The cross-sectional image of the PD and elemental composition of Pt-doped Si was characterized using SEM (Tescan, Mira 3XH) and energy-dispersive x-ray spectroscopy (EDS; Oxford instruments, AZtec X-Max[N] 80). The SWIR absorption spectra were measured using a NIR spectrometer (Ideaoptics, NIR2500). The photoelectric response of the PD was measured at room temperature using a source meter (Keithley, SMU2400) under illumination of a 1319 nm laser (CNI lase, MIL-H-1319). The defect level positions of Pt-doped Si were measured with deep level transient spectroscopy (DLTS; PhysTech, FT1230). The bandgap of ZnO was tested by photoluminescence spectroscopy (PL; Ocean Optics, USB2000) excited with a 325 nm He-Cd laser beam at room temperature. The valence band minimum of ZnO was measured with ultraviolet photoelectron spectroscopy (UPS; Thermo Fisher, Escalab Xi+). The series resistance of the PD was determined using a solar simulator (Oriel/Newport, 94023A). The crystallinity of ZnO was characterized with grazing incidence x-ray diffraction spectra (GIXRD) by using an x-ray diffractometer (Rigaku, SmartLab 9 kW).

We started our experiment by examining the SWIR optical properties of Pt-doped Si. Pt was selected as the dopant due to its high solubility and fast diffusion in Si.[41] To verify the diffusion of Pt into Si, a 10 nm thick Pt layer was sputtered on the backside of the double-sided polished Si and then annealed in nitrogen at 950 °C for 30 min. Then, Pt elemental distribution was checked on the front side of the Si using EDS mapping. As shown in Fig. 2(a), Pt is detectable as marked yellow spots, indicating that Pt has diffused well into the Si matrix and even reached the other side of the Si substrate. With thermal annealing, Pt atoms diffuse in Si following the Frank–Turnbull mechanism, which postulates that interstitial Pt atoms become substitutional by occupying vacant lattice sites.[42,43] Additionally, the substitutional atoms will form stable bulk defects in Si, providing defect levels for SWIR absorption.[44,45] Figure 2(b) shows the absorption spectra of the Si substrate and Pt-doped Si in the SWIR wavelength region. The average SWIR absorption of the Si is less than 5% beyond the 1100 nm wavelength due to the 1.12 eV bandgap of Si. However, with Pt doping, the SWIR absorption of Si increased to an average of about 50%.

After depositing electrodes on the front and back of the Pt-doped Si samples, the photoelectric response characteristics were measured. The applied bias voltage has ITO as the positive electrode and Al as the negative electrode. Figure 3 depicts the dark current density and photocurrent density of the Pt-doped Si PD. With negative bias, the I–V curve appears almost linear, indicating that the Pt-doped Si PD is of photoconductive type.[46] As seen in Fig. 3, the dark current of the PD is comparatively high, which is a typical drawback of the BDA PD.[20,25,28] For unambiguous comparisons, all measurements of PD in this work were conducted at the same bias of −1 V. For this PD, the dark current density at −1 V is $1.30 \times 10^{-5} \, A/cm^2$, and the photocurrent density is $1.72 \times 10^{-5} \, A/cm^2$ at 1319 nm light illumination with an incident power of 17 mW.

The dark current of the Pt-doped Si PD is primarily due to the bulk defect levels, constituting additional transport channels for electrons. Under bias, electrons can transport through the defect levels, resulting in a substantial increase in dark current.[47,48] Emulating the BIB detector, a blocking layer is introduced to the PD to impede the transport of these electrons. The material of the blocking layer must fulfill the following requirements simultaneously:
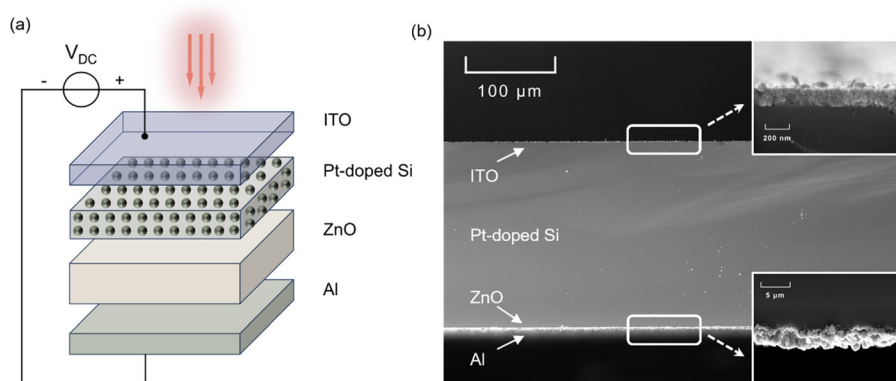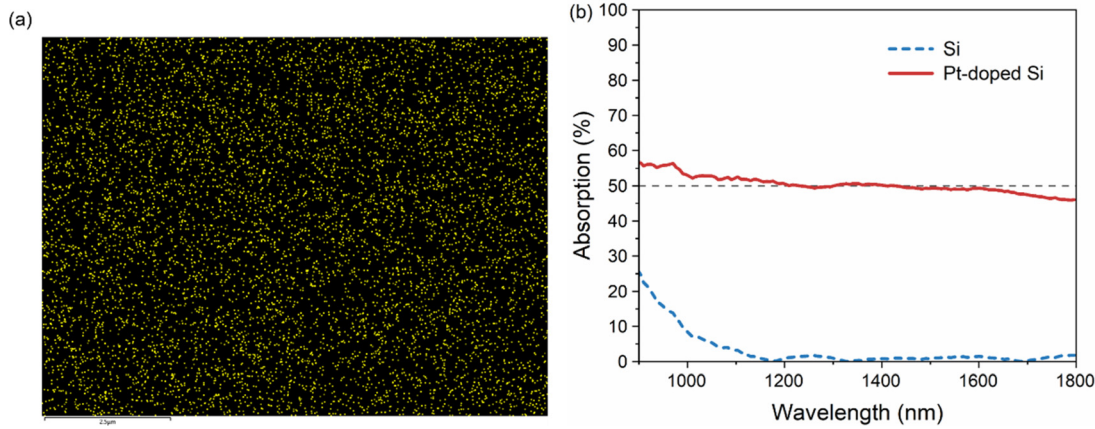

FIG. 1. Schematic illustration (a) and cross-sectional SEM image (b) of the PD.

FIG. 2. (a) EDS map of Pt on one side of n-Si wafer opposite to where Pt was deposited after Pt diffusion. The yellow spots describe the distribution of Pt atoms. (b) Absorption spectra of Si and Pt-doped Si samples.

(i) Wide bandgap. The bandgap of the blocking layer should be wide enough to fully cover the defect levels formed by the Pt doping in Si.

(ii) Proper band alignment. The CBM of the blocking layer should align closely with or lower than that of Si, ensuring minimal interference with the photocurrent.

The DLTS indicates that the primary defect level formed by Pt in Si is located at 0.22 eV below the conduction band, equivalent to −4.27 eV relative to the vacuum level, which is consistent with the value reported.[49,50] After considering requirements (i) and (ii), we chose ZnO as the material for the blocking layer, which possesses a wide bandgap of approximately 3.2 eV,[36] significantly wider than Si (1.12 eV). Additionally, the CBM of ZnO is around −4.2 eV, which is slightly lower than that of Si (−4.05 eV) but higher than the primary defect level formed by Pt in Si. Therefore, we deposited ZnO between the Pt-doped Si and Al electrode of the PD as the blocking layer of dark current, as shown in Fig. 1(a).
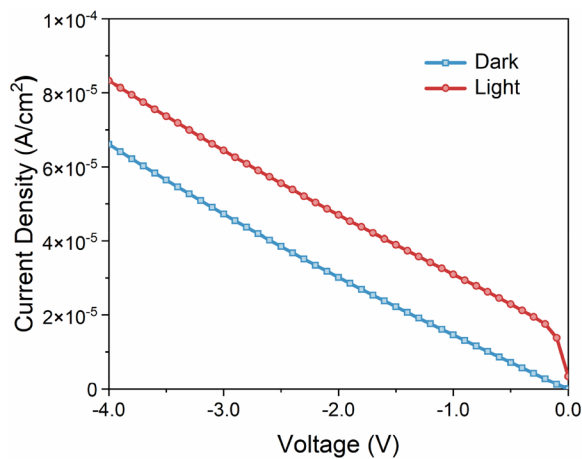
FIG. 3. Dark current and photocurrent densities of the Pt-doped Si PD without the blocking layer under 1319 nm light illumination with an incident power of 17 mW.

To verify the energy levels of ZnO, we conducted PL and UPS measurements, determining the bandgap of 3.28 eV and valence band maximum of −7.52 eV for ZnO. Therefore, the calculated CBM for ZnO is −4.24 eV, closely aligned with the values reported. The energy diagram of the PD is displayed in Fig. 4. Under illumination, electrons on these defect levels can absorb SWIR with wavelengths over 1100 nm, be excited to the conduction band, and form photocurrent.[19,20] With the ZnO blocking layer, the dark current from the defect levels can be blocked. Since the CBM of ZnO is slightly lower than that of Si, the transport of photocurrent is hardly affected. The ZnO blocking layer can significantly reduce dark current without markedly affecting the photoresponse of the PD, thereby improving PD detection.

Figure 5(a) shows the dark current densities and responsivities of PDs with different thicknesses of the ZnO blocking layers. There is a substantial decrease in the dark current after adding the ZnO blocking layer. Table I lists the dark current densities, responsivities, specific detectivities, and series resistances of PDs with various thicknesses of ZnO at 1319 nm. The annealing temperature of ZnO is 600 °C. The specific detectivity of PD limited by shot noise is determined by[51,52]

$$D^* = \frac{R\sqrt{A}}{\sqrt{2qI_d}}, \qquad (1)$$

where R is the responsivity, as defined by dividing the photocurrent by the incident light power, I_d is the dark current, q is the electron charge, and A is the device area, which is 1 cm^2 for all the PDs in this work. With the increasing thickness of the ZnO blocking layer, the dark current of the PD is decreased, which is attributed to the reduced tunneling probability of electrons from the bulk defect levels through the blocking layer. On the other hand, the increasing series resistance of ZnO also contributes to the decrease in the dark current. In the meantime, it is seen that the responsivity of the PD also decreased as shown in Fig. 5(b), which is attributed to the increased series resistance of ZnO.

A 40 nm-thick ZnO blocking layer was chosen in terms of the maximal specific detectivity. With the 40 nm ZnO blocking layer, the dark current density at −1 V is decreased from 1.30×10^{-5} to
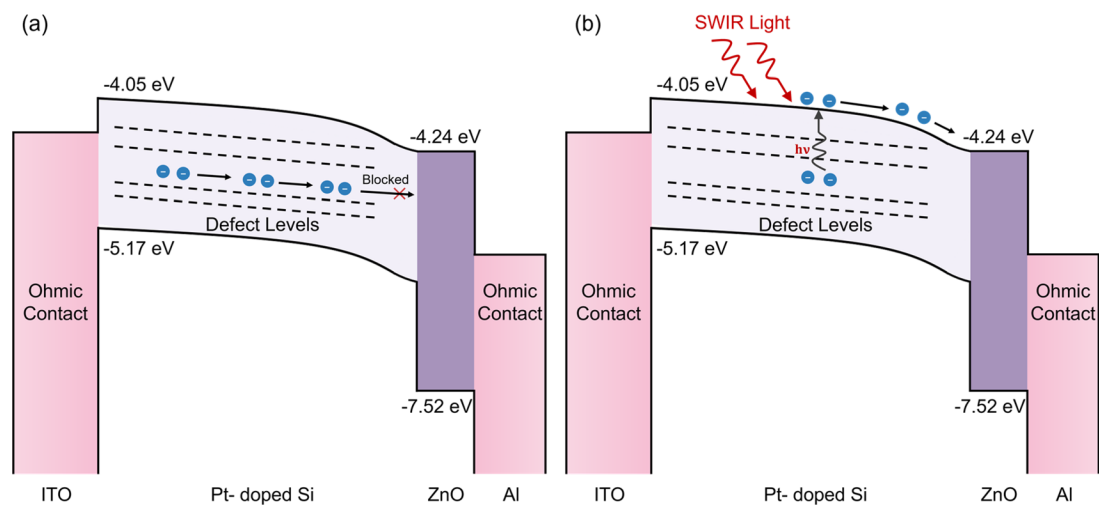
FIG. 4. Energy diagram of PD incorporated with ZnO blocking layer: (a) in dark condition and (b) under illumination.
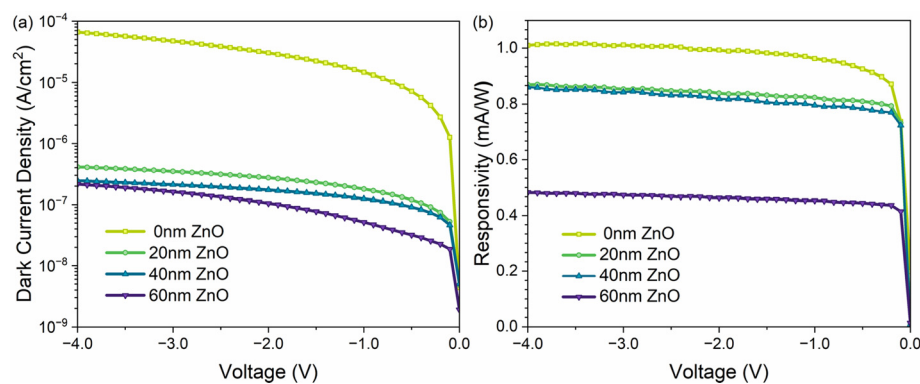

FIG. 5. (a) Dark current densities of the PDs with ZnO blocking layers of different thicknesses annealed at 600 °C. (b) Responsivities of the PDs with ZnO blocking layers of different thicknesses annealed at 600 °C under 1319 nm light illumination with an incident power of 17 mW.

1.22×10^{-7} A/cm^2, dropping by two orders of magnitude, while the responsivity changes only from 1.01 to 0.81 mA/W. Therefore, the specific detectivity increases by one order of magnitude from 4.96×10^{8} to 4.10×10^{9} cm·(Hz)$^{1/2}$/W, or Jones.

We also studied the impact of the annealing temperature of ZnO on PD performance. The samples with 40 nm ZnO blocking layers were annealed in nitrogen at temperatures of 500, 600, and 700 °C for 30 min, respectively. As shown in Fig. 6(a), the dark current densities of the PDs with ZnO annealed at 500, 600, and 700 °C are 7.75×10^{-7},

1.22×10^{-7}, and 2.14×10^{-7} A/cm^2 at -1 V, respectively. Compared to the PD annealed at 500 °C, the dark current of the PD annealed at 600 °C is significantly decreased, which could be attributed to the improved crystalline quality of ZnO.[53,54] Figure 7 shows the GIXRD spectra of the ZnO with different annealing temperatures. At any annealing temperature, the (100), (002), and (101) diffraction peaks indexed to the hexagonal wurtzite ZnO (JPCDS: 36-1451) are prominent, indicating the high crystallinity of the ALD-grown ZnO thin films, which naturally have polycrystalline characteristics.[55] As the

TABLE I. Performance comparison of the PDs with ZnO blocking layers of different thicknesses at a bias of -1 V under 1319 nm light illumination with an incident power of 17 mW.

Thickness of the ZnO blocking layer (nm)	Dark current density (A/cm^2)	Responsivity (mA/W)	Specific detectivity (Jones)	Series resistance (Ω)
0	1.30×10^{-5}	1.01	4.96×10^{8}	278
20	1.66×10^{-7}	0.86	3.73×10^{9}	317
40	1.22×10^{-7}	0.81	4.10×10^{9}	336
60	4.61×10^{-8}	0.45	3.73×10^{9}	406
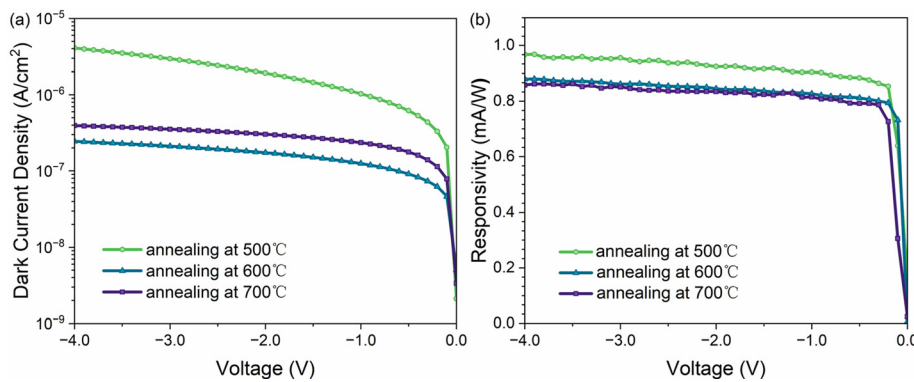
FIG. 6. (a) Dark current densities of the PDs with 40 nm ZnO blocking layers at different annealing temperatures. (b) Responsivities of the PDs with 40 nm ZnO blocking layers at different annealing temperatures under 1319 nm light illumination with an incident power of 17 mW.
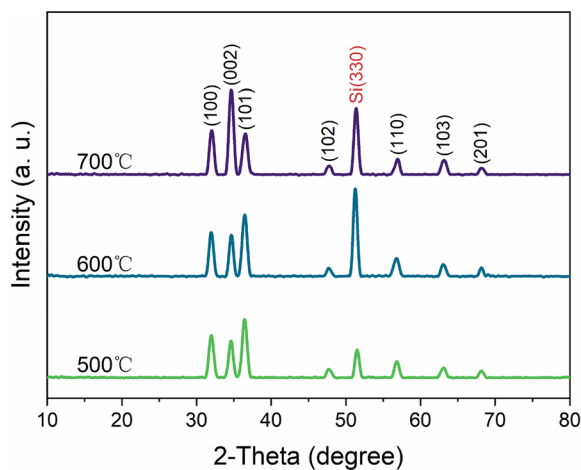
FIG. 7. GIXRD spectra of ZnO at different annealing temperatures. The red-marked (3 3 0) diffraction peak originates from the Si substrate.

annealing temperature increases, higher intensities and smaller widths of the diffraction peaks, especially for the (002) diffraction peak, confirm that the crystallinity of ZnO is further enhanced. However, further increasing the annealing temperature of ZnO to 700 °C causes a slight increase in the dark current. This is attributed to the increase in the grain size of ZnO as the annealing temperature rises, leading to an

increase in surface roughness.[54] The responsivities of PDs remain generally consistent with different annealing temperatures shown in Fig. 6(b), indicating that the annealing temperature of ZnO changes its CBM very minimally. Overall, Figs. 6(a) and 6(b) show PD performance reached its optimum at an annealing temperature of 600 °C.

In terms of the requirements (i) and (ii) of the blocking layer mentioned earlier, we have also testified TiO_2 and WO_3. Their energy levels relative to Si are plotted in Fig. 8. We fabricated PDs with TiO_2 and WO_3 blocking layers that have the same thickness and annealing conditions. Figure 9 shows the dark current densities and responsivities of PDs with different oxides of the blocking layer including ZnO, TiO_2, and WO_3, respectively. The responsivities and specific detectivities are shown in Table II. For the TiO_2 blocking layer, the dark current density exhibits a comparable order of magnitude decrease to that with the ZnO one, as TiO_2 has similar bandgap width and CBM positions to those of ZnO. However, the responsivity of the PD with the TiO_2 blocking layer is only about 60% of that with ZnO, which is possibly due to the higher resistivity than ZnO.[56,57] The measured series resistance of the PD with the TiO_2 blocking layer is 391 Ω, higher than that with ZnO. The dark current of the PD with the WO_3 blocking layer, however, exhibits only a marginal dark current decrease compared to the PD without the blocking layer. As illustrated in Fig. 8, since the CBM of WO_3 is lower than ZnO and TiO_2, the primary defect level at −4.27 eV formed by the doping of Pt in Si cannot be covered by the bandgap of WO_3. Consequently, the probability of the electrons transporting from the defect levels through the WO_3 layer is hardly reduced.

FIG. 8. Energy diagram of oxides relative to Pt-doped Si: (a) ZnO; (b) TiO_2; and (c) WO_3. The energy levels of oxides are cited from Grätzel.[38]

24 October 2024 08:46:28

FIG. 9. (a) Dark current densities of the PD with 40 nm ZnO, TiO$_2$, and WO$_3$ blocking layers annealed at 600 °C, respectively. (b) Responsivities of the PD with 40 nm ZnO, TiO$_2$, and WO$_3$ blocking layers annealed at 600 °C under 1319 nm light illumination with an incident power of 17 mW, respectively.
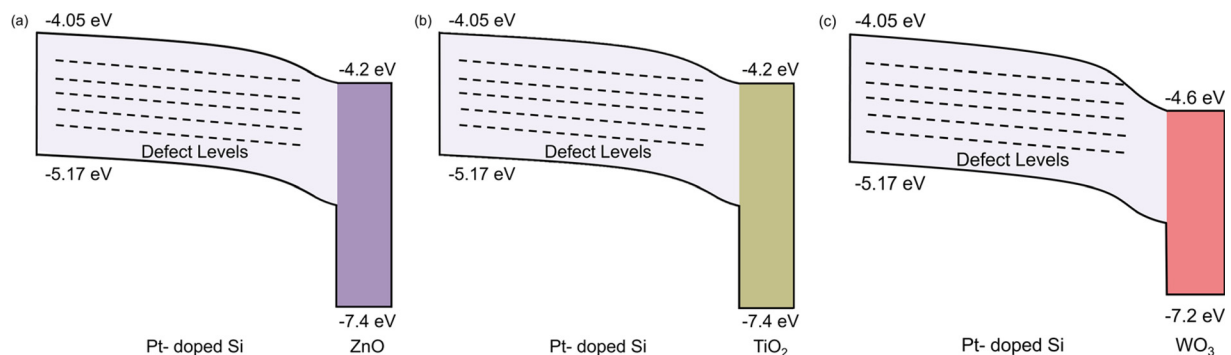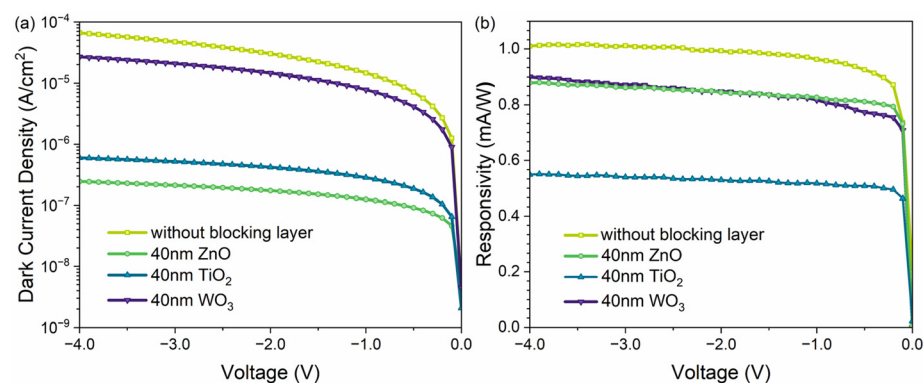
TABLE II. Performance comparison of the PD with blocking layers of different oxides at a bias of −1 V under 1319 nm light illumination with an incident power of 17 mW.

Oxide of the blocking layer	Dark current density (A/cm^2)	Responsivity (mA/W)	Specific detectivity (Jones)
None	1.30×10^{-5}	1.01	4.96×10^{8}
ZnO	1.22×10^{-7}	0.81	4.10×10^{9}
TiO$_2$	2.91×10^{-7}	0.50	1.63×10^{9}
WO$_3$	7.81×10^{-6}	0.89	5.65×10^{8}

TABLE III. Performance comparison of other PDs and ours.

PD	Measure wavelength (nm)	Dark current or dark current density	Responsivity	Specific detectivity (Jones)
This work without blocking layer	1319	1.30×10^{-5} A/cm^2	1.01 mA/W	4.96×10^{8}
This work with blocking layer	1319	1.22×10^{-7} A/cm^2	0.81 mA/W	4.10×10^{9}
This work with textured Si and blocking layer	1319	4.93×10^{-8} A/cm^2	2.65 mA/W	2.11×10^{10}
Se-doped Si p-n photodiode[26]	1550	57.3 μA	50 μA/W	· · ·
S-doped Si photodiode[28]	1330	0.12 mA	50 mA/W	· · ·
Ar-hyperdoped Si n$^+$-n photodiode[27]	1310	· · ·	0.975 A/W	1.14×10^{10}
Laser-modified Si photodetector[58]	1310	1.36×10^{-4} A/cm^2	0.26 A/W	· · ·

To highlight the effect of the blocking layer, planar Si has been chosen as the substrate in this work. To further enhance the responsivity and detectivity of the PD, we also fabricated the PD with passivated textured Si as the substrate and compared its performance parameters with other similar BDA-type PDs as shown in Table III. It is seen that our device features a lower dark current after applying the blocking layer, although responsivities are different among those PDs.

In summary, a blocking layer of dark current is applied to the SWIR BDA PD to impede the transport of electrons from the bulk defect levels. SWIR photoelectric response is provided by the bulk defect levels formed by Pt doping in Si. By introducing a ZnO blocking layer to the PD, the dark current density is reduced from 1.30×10^{-5} to 1.22×10^{-7} A/cm^2, and the specific detectivity is enhanced from 4.96×10^{8} to 4.10×10^{9} Jones at room temperature. The optimal thickness and annealing temperature of the ZnO blocking layer have been determined. The effects of TiO$_2$ and WO$_3$ as the blocking layers were also compared with those of ZnO. This research provides a simple and effective method for suppressing the dark current and enhancing the detectivity in SWIR photodetection of BDA type.

AUTHOR DECLARATIONS
Conflict of Interest

The authors have no conflicts to disclose.

Author Contributions

Liang Yu: Conceptualization (lead); Data curation (lead); Investigation (lead); Methodology (lead); Project administration (lead); Validation (lead); Writing – original draft (lead); Writing – review & editing

(lead). **Li Wu:** Investigation (equal); Validation (equal). **Xiyuan Dai:** Validation (equal). **Yanru Yang:** Validation (equal). **Zhongyao Yan:** Visualization (equal). **Kaixin Liu:** Validation (equal). **Fengyang Ma:** Validation (equal). **Ming Lu:** Conceptualization (equal); Funding acquisition (equal); Resources (equal); Supervision (equal); Writing – review & editing (equal). **Jian Sun:** Conceptualization (equal); Funding acquisition (equal); Resources (equal); Supervision (equal); Writing – review & editing (equal).

DATA AVAILABILITY

The data that support the findings of this study are available from the corresponding authors upon reasonable request.

REFERENCES

[1]B. Jalali and S. Fathpour, "Silicon photonics," J. Lightwave Technol. **24**(12), 4600–4615 (2006).

[2]R. Won, "Integrating silicon photonics," Nat. Photonics **4**(8), 498–499 (2010).

[3]Y.-C. Huang, V. Parimi, W.-C. Chang, H.-J. Syu, Z.-C. Su, and C.-F. Lin, "Silicon-based photodetector for infrared telecommunication applications," IEEE Photonics J. **13**(2), 1–7 (2021).

[4]M. Tanzid, A. Ahmadivand, R. Zhang, B. Cerjan, A. Sobhani, S. Yazdi, P. Nordlander, and N. J. Halas, "Combining plasmonic hot carrier generation with free carrier absorption for high-performance near-infrared silicon-based photodetection," ACS Photonics **5**(9), 3472–3477 (2018).

[5]J.-M. Choi, H. Y. Jang, A. R. Kim, J.-D. Kwon, B. Cho, M. H. Park, and Y. Kim, "Ultra-flexible and rollable 2D-MoS$_2$/Si heterojunction-based near-infrared photodetector via direct synthesis," Nanoscale **13**(2), 672–680 (2021).

[6]H. Anabestani, S. Nabavi, and S. Bhadra, "Advances in flexible organic photodetectors: Materials and applications," Nanomaterials **12**(21), 3775 (2022).

[7]M. Casalino, G. Coppola, R. M. De La Rue, and D. F. Logan, "State-of-the-art all-silicon sub-bandgap photodetectors at telecom and datacom wavelengths," Laser Photonics Rev. **10**(6), 895–921 (2016).

[8]F. Cao, L. Liu, and L. Li, "Short-wave infrared photodetector," Mater. Today **62**, 327–349 (2023).

[9]A.-T. Jhang, P.-C. Tsai, Y.-T. Tsai, S.-Y. Lin, and M.-H. Fang, "Quantum-dots-in-double-perovskite for high-gain short-wave infrared photodetector," Adv. Opt. Mater. 2401252 (2024).

[10]J. Xiong, Q. Yu, X. Hou, B. Liu, S. Li, H. Deng, Z. Yang, J. Leng, S. Zhu, Y. Sun, Z. Jiang, N. Huo, J. Wu, and P. Zhou, "Short-wave infrared photodetectors based on β-In$_2$Se$_3$/Te heterojunctions for optical communication and polarimetric imaging applications," Adv. Funct. Mater. **34**(26), 2314972 (2024).

[11]Z. Ren, P. Wang, K. Zhang, W. Ran, J. Yang, Y. Liu, Z. Lou, G. Shen, and Z. Wei, "Short-wave near-infrared polarization sensitive photodetector based on GaSb nanowire," IEEE Electron Device Lett. **42**(4), 549–552 (2021).

[12]Y. Xu, C. Liu, C. Guo, Q. Yu, W. Guo, W. Lu, X. Chen, L. Wang, and K. Zhang, "High performance near infrared photodetector based on in-plane black phosphorus p-n homojunction," Nano Energy **70**, 104518 (2020).

[13]J. P. Mailoa, A. J. Akey, C. B. Simmons, D. Hutchinson, J. Mathews, J. T. Sullivan, D. Recht, M. T. Winkler, J. S. Williams, J. M. Warrender, P. D. Persans, M. J. Aziz, and T. Buonassisi, "Room-temperature sub-band gap opto-electronic response of hyperdoped silicon," Nat. Commun. **5**(1), 3011 (2014).

[14]M. Casalino, G. Coppola, M. Iodice, I. Rendina, and L. Sirleto, "Near-infrared sub-bandgap all-silicon photodetectors: State of the art and perspectives," Sensors **10**(12), 10571–10600 (2010).

[15]H. Chen, X. Luo, and A. W. Poon, "Cavity-enhanced photocurrent generation by 1.55 μm wavelengths linear absorption in a pin diode embedded silicon microring resonator," Appl. Phys. Lett. **95**, 171111 (2009).

[16]X. Li, Z. Deng, J. Li, Y. Li, L. Guo, Y. Jiang, Z. Ma, L. Wang, C. Du, Y. Wang, Q. Meng, H. Jia, W. Wang, W. Liu, and H. Chen, "Hybrid nanoscale Au with ITO structure for a high-performance near-infrared silicon-based photodetector with ultralow dark current," Photonics Res. **8**(11), 1662–1670 (2020).

[17]T. Tanabe, H. Sumikura, H. Taniyama, A. Shinya, and M. Notomi, "All-silicon sub-Gb/s telecom detector with low dark current and high quantum efficiency on chip," Appl. Phys. Lett. **96**, 101103 (2010).

[18]J. Kim, L. J. Krayer, J. L. Garrett, and J. N. Munday, "Interfacial defect-mediated near-infrared silicon photodetection with metal oxides," ACS Appl. Mater. Interfaces **11**(50), 47516–47524 (2019).

[19]C. Li, J.-H. Zhao, Y. Yang, Q.-D. Chen, Z.-G. Chen, and H.-B. Sun, "Sub-bandgap photo-response of chromium hyperdoped black silicon photodetector fabricated by femtosecond laser pulses," IEEE Sens. J. **21**(22), 25695–25702 (2021).

[20]L. Wu, L. Yu, X. Dai, F. Ma, S. Wang, M. Lu, and J. Sun, "Bulk defect-mediated absorption sub-bandgap all-silicon photodetector with low dark current density at ambient temperatures," ACS Photonics **10**(10), 3674–3681 (2023).

[21]M. V. Limaye, S. C. Chen, C. Y. Lee, L. Y. Chen, S. B. Singh, Y. C. Shao, Y. F. Wang, S. H. Hsieh, H. C. Hsueh, J. W. Chiou, C. H. Chen, L. Y. Jang, C. L. Cheng, W. F. Pong, and Y. F. Hu, "Understanding of sub-band gap absorption of femtosecond-laser sulfur hyperdoped silicon using synchrotron-based techniques," Sci. Rep. **5**, 11466 (2015).

[22]M. Wang, Y. Berencén, E. García-Hemme, S. Prucnal, R. Hübner, Y. Yuan, C. Xu, L. Rebohle, R. Böttger, R. Heller, H. Schneider, W. Skorupa, M. Helm, and S. Zhou, "Extended infrared photoresponse in Te-hyperdoped Si at room temperature," Phys. Rev. Appl. **10**(2), 024054 (2018).

[23]M. Wang, E. García-Hemme, Y. Berencén, R. Hübner, Y. Xie, L. Rebohle, C. Xu, H. Schneider, M. Helm, and S. Zhou, "Silicon-based intermediate-band infrared photodetector realized by Te hyperdoping," Adv. Opt. Mater. **9**(4), 2001546 (2021).

[24]C. Li, J.-H. Zhao, and Z.-G. Chen, "Infrared absorption and sub-bandgap photo-response of hyperdoped silicon by ion implantation and ultrafast laser melting," J. Alloys Compd. **883**, 160765 (2021).

[25]M.-J. Sher and E. G. Hemme, "Hyperdoped silicon materials: From basic materials properties to sub-bandgap infrared photodetectors," Semicond. Sci. Technol. **38**(3), 033001 (2023).

[26]Y. Berencén, S. Prucnal, F. Liu, I. Skorupa, R. Hübner, L. Rebohle, S. Zhou, H. Schneider, M. Helm, and W. Skorupa, "Room-temperature short-wavelength infrared Si photodetector," Sci. Rep. **7**, 43688 (2017).

[27]C. Li, J.-H. Zhao, X.-H. Liu, Z.-Y. Ren, Y. Yang, Z.-G. Chen, Q.-D. Chen, and H.-B. Sun, "Record-breaking-high-responsivity silicon photodetector at infrared 1.31 and 1.55 μm by argon doping technique," IEEE Trans. Electron Devices **70**(5), 2364–2369 (2023).

[28]J. E. Carey, C. H. Crouch, M. Shen, and E. Mazur, "Visible and near-infrared responsivity of femtosecond-laser microstructured silicon photodiodes," Opt. Lett. **30**(14), 1773–1775 (2005).

[29]M. D. Petroff and M. G. Stapelbroek, "Blocked impurity band detectors," U.S. Patent 4,568,960 (4 February 1986).

[30]J. E. Huffman, A. G. Crouse, B. L. Halleck, T. V. Downes, and T. L. Herter, "Si: Sb blocked impurity band detectors for infrared astronomy," J. Appl. Phys. **72**(1), 273–275 (1992).

[31]H. Zhu, J. Zhu, W. Hu, Y. Xiao, J. Shen, Q. Li, K. Zhang, K. Deng, T. He, H. Wu, N. Li, and W. Lu, "Temperature-sensitive mechanism for silicon blocked-impurity-band photodetectors," Appl. Phys. Lett. **119**, 191104 (2021).

[32]M. Hanaoka, H. Kaneda, S. Oyabu, M. Yamagishi, Y. Hattori, S. Ukai, K. Shichi, T. Wada, T. Suzuki, K. Watanabe, K. Nagase, S. Baba, and C. Kochi, "Development of blocked-impurity-band-type Ge detectors fabricated with the surface-activated wafer bonding method for far-infrared astronomy," J. Low Temp. Phys. **184**, 225–230 (2016).

[33]J. W. Beeman, S. Goyal, L. A. Reichertz, and E. E. Haller, "Ion-implanted Ge: B far-infrared blocked-impurity-band detectors," Infrared Phys. Technol. **51**(1), 60–65 (2007).

[34]K. Deng, K. Zhang, Q. Li, T. He, Y. Xiao, J. Guo, T. Zhang, H. Zhu, P. Wang, N. Li, and W. Hu, "High-operating temperature far-infrared Si: Ga blocked-impurity-band detectors," Appl. Phys. Lett. **120**, 211103 (2022).

[35]H. Carchano and C. Jund, "Electrical properties of silicon doped with platinum," Solid-State Electron. **13**(1), 83–90 (1970).

[36]A. Hagfeldt and M. Graetzel, "Light-induced redox reactions in nanocrystalline systems," Chem. Rev. **95**(1), 49–68 (1995).

[37]C. G. Van de Walle and J. Neugebauer, "Universal alignment of hydrogen levels in semiconductors, insulators and solutions," Nature **423**(6940), 626–628 (2003).

[38]M. Grätzel, "Photoelectrochemical cells," Nature **414**(6861), 338–344 (2001).

[39]G. Gould and E. A. Irene, "The influence of silicon surface cleaning procedures on silicon oxidation," J. Electrochem. Soc. **134**(4), 1031 (1987).

[40]A. R. Martin, M. Baeyens, W. Hub, P. W. Mertens, and B. O. Kolbesen, "Alkaline cleaning of silicon wafers: Additives for the prevention of metal contamination," Microelectron. Eng. **45**(2-3), 197–208 (1999).

[41]S. Mantovani, F. Nava, C. Nobili, and G. Ottaviani, "In-diffusion of Pt in Si from the PtSi/Si interface," Phys. Rev. B **33**(8), 5536 (1986).

[42]W. Lerch, N. A. Stolwijk, H. Mehrer, and C. Poisson, "Diffusion of platinum into dislocated and non-dislocated silicon," Semicond. Sci. Technol. **10**(9), 1257 (1995).

[43]E. Badr, P. Pichler, and G. Schmidt, "Modeling platinum diffusion in silicon," J. Appl. Phys. **116**, 133508 (2014).

[44]H. Zimmermann and H. Ryssel, "Gold and platinum diffusion: The key to the understanding of intrinsic point defect behavior in silicon," Appl. Phys. A **55**, 121–134 (1992).

[45]K. P. Lisiak and A. G. Milnes, "Energy levels and concentrations for platinum in silicon," Solid-State Electron. **18**(6), 533–540 (1975).

[46]H. Beneking, "Gain and bandwidth of fast near-infrared photodetectors: A comparison of diodes, phototransistors, and photoconductive devices," IEEE Trans. Electron Devices **29**(9), 1420–1431 (1982).

[47]C. Pan, Z. Yin, Z. Song, Y. Yao, Y. Zhang, J. Hao, T. Kang, H. Deng, H. Wu, and N. Dai, "Dark-current-blocking mechanism in BIB far-infrared detectors by interfacial barriers," IEEE Trans. Electron Devices **68**(6), 2804–2809 (2021).

[48]S. Luo, J. L. Li, T. Sun, X. Liu, D. Wei, D. Zhou, J. Shen, and D. Wei, "High-performance mid-infrared photodetection based on Bi$_2$Se$_3$ maze and free-standing nanoplates," Nanotechnology **32**(10), 105705 (2020).

[49]S. D. Brotherton, P. Bradley, and J. Bicknell, "Electrical properties of platinum in silicon," J. Appl. Phys. **50**(5), 3396–3403 (1979).

[50]K. P. Lisiak and A. G. Milnes, "Platinum as a lifetime-control deep impurity in silicon," J. Appl. Phys. **46**(12), 5229–5235 (1975).

[51]W. Choi, M. Y. Cho, A. Konar, J. H. Lee, G.-B. Cha, S. C. Hong, S. Kim, J. Kim, D. Jena, J. Joo, and S. Kim, "High-detectivity multilayer MoS$_2$ phototransistors with spectral response from ultraviolet to infrared," Adv. Mater. **24**(43), 5832–5836 (2012).

[52]G.-X. Liang, C.-H. Li, J. Zhao, Y. Fu, Z.-X. Yu, Z.-H. Zheng, Z.-H. Su, P. Fan, X.-H. Zhang, J.-T. Luo, L. Ding, and S. Chen, "Self-powered broadband kesterite photodetector with ultrahigh specific detectivity for weak light applications," SusMat **3**(5), 682–696 (2023).

[53]C.-Y. Yen, S.-R. Jian, G.-J. Chen, C.-M. Lin, H.-Y. Lee, W.-C. Ke, Y.-Y. Liao, P.-F. Yang, C.-T. Wang, Y.-S. Lai, J. S.-C. Jang, and J.-Y. Juang, "Influence of annealing temperature on the structural, optical and mechanical properties of ALD-derived ZnO thin films," Appl. Surf. Sci. **257**(17), 7900–7905 (2011).

[54]J. Lim and C. Lee, "Effects of substrate temperature on the microstructure and photoluminescence properties of ZnO thin films prepared by atomic layer deposition," Thin Solid Films **515**(7-8), 3335–3338 (2007).

[55]J. Iqbal, A. Jilani, P. M. Z. Hassan, S. Rafique, R. Jafer, and A. A. Alghamdi, "ALD grown nanostructured ZnO thin films: Effect of substrate temperature on thickness and energy band gap," J. King Saud Univ. Sci. **28**(4), 347–354 (2016).

[56]H. Beh, D. Hiller, and M. Zacharias, "Optimization of ALD-ZnO thin films toward higher conductivity," Phys. Status Solidi A **215**(16), 1700880 (2018).

[57]A. S. Babadi, R. Tang-Kong, and P. C. McIntyre, "Link between gas phase reaction chemistry and the electronic conductivity of atomic layer deposited titanium oxide thin films," J. Phys. Chem. Lett. **12**(14), 3625–3632 (2021).

[58]J.-H. Zhao, C.-H. Li, X.-B. Li, Q.-D. Chen, Z.-G. Chen, and H.-B. Sun, "NIR photodetector based on nanosecond laser-modified silicon," IEEE Trans. Electron Devices **65**(11), 4905–4909 (2018).